Electro-thermal Modeling and Design of High-current Pulse Power Supply for Electrically Assisted Manufacturing

Wu, Jiawei; Han, Xiaotao; Wang, Huai

Published in:
IEEE Access

DOI (link to publication from Publisher):
10.1109/ACCESS.2019.2949586

Publication date:
2019

Document Version
Publisher's PDF, also known as Version of record

IEEE Access
Multidisciplinary | Rapid Review | Open Access Journal

Received October 3, 2019, accepted October 19, 2019, date of publication October 25, 2019, date of current version November 14, 2019.

Digital Object Identifier 10.1109/ACCESS.2019.2949586

Electro-Thermal Modeling and Design of High-Current Pulse Power Supply for Electrically Assisted Manufacturing

JIAWEI WU[1,2,4], XIAOTAO HAN[1,2], (Member, IEEE), AND HUAI WANG[3,4], (Senior Member, IEEE)

[1]Wuhan National High Magnetic Field Center, Huazhong University of Science and Technology, Wuhan 430074, China
[2]State Key Laboratory of Advanced Electromagnetic Engineering and Technology, Huazhong University of Science and Technology, Wuhan 430074, China
[3]School of Electronics and Information, Yangtze University, Jingzhou 434023, China
[4]Department of Energy Technology, Aalborg University, 9220 Aalborg, Denmark

Corresponding author: Huai Wang (hwa@et.aau.dk)

ABSTRACT Electrically assisted manufacturing (EAM) is a promising and rapidly developing metal processing method. The power supply is a key sub-system for EAM, which needs to be designed properly. This paper proposes the model-based design of a low-voltage high-current pulse power supply used for EAM based on converter-level electro-thermal modeling. The thermal stress of key components is obtained by converter-level finite element simulations. A simplified thermal modeling method is proposed to reduce the computation burden of the FEM simulation to obtain the dynamic thermal profile under pulse current operation. The impact of the duration of the current pulse on the maximum temperature and temperature variations of MOSFETs is investigated based on the thermal model. A case study of a 10 V/500 A pulse power supply is presented to demonstrate the theoretical analyses and verification. The outcomes contribute to the design optimization and virtual prototyping of pulse power supplies for EAM applications.

INDEX TERMS Electrically assisted manufacturing, electro-thermal modeling, finite element analysis, thermal model, virtual prototyping.

I. INTRODUCTION

Electrically assisted manufacturing (EAM) is an enhanced metal forming process by applying direct electric current or electric field on forming material. The enhancement includes a reduction in flow stress during forming, increased ductility and decreased elastic recovery through residual stress elimination [1], [2]. It is already found beneficial to various forming processes [3]. The complex effect of electricity on metals is known as electroplastic effect (EPE) [4], and is observed various metals and alloys, including stainless steel [5], aluminum alloy [6], magnesium alloy [7], nanocrystalline, and amorphous alloys [8]. The research of EPE has great significance in improving the formability of lightweight materials in room temperature, in which lightweight materials have a poor formability using conventional forming methods. However, the mechanism and effect of EPE in metal alloys is not fully understood. More research should be carried out to illustrate the mechanism and effect of EPE before EAM can be widely used in industrial production. The research of EAM and EPE has a significant impact on the promotion of lightweight metal manufacturing, especially in the aerospace and automotive industries.

The electric current acts on EAM is directly applied to both ends of the resistive load during the forming process. The current can be both constant and pulsed current. A square wave is the most commonly used of current loading. The nominal current density varies from 6 to 180 A/mm^2 in [1], [6]. An advanced concept, electric energy density is proposed based on the concept of nominal current density in [9]. It is demonstrated that the pulse duration is also responsible for the flow stress drop.

Besides the efficiency, thermal modeling and design is an essential aspect of such pulse power supplies. The degradation and failure of key components, such as capacitors, and semiconductor switches, are sensitive to

The associate editor coordinating the review of this manuscript and approving it for publication was Yijie Wang.

temperature [10], [11]. Moreover, the temperature variation induced by the pulse operation should also be considered since semiconductor switches have a limited thermal cycle capability [12].

In previous EAM research and EPE experiments [1], [3], [13], little attention has been paid to the design and optimization of the current generator. Especially the reliability and thermal performance of the power supply are usually not considered while in the design stage. As EAM technique becomes increasingly mature and has great potential in industrial applications, the platform for EAM should co-developed to provide a technical basis for the application.

Electro-thermal design is usually done to ensure the power device or the designed system can operate safely in the required working environment without building prototypes. It is widely used in the design of high-power devices. Most of the previous researches of electro-thermal design were done for devices operating in a stable output [14]–[16]. The analysis of stable thermal stress is sufficient. For the special application of EAM and EPE experiments, the power supply operates in a square-wave mode with short turn-on time and small duty cycle. Transient temperature variation should be analyzed. No discussion is done about pulse output equipment in previous researches. Compared with steady-state simulation, the computation burden of transient simulation increases with the number of the time point, which may reach hundreds of times of steady-state simulation. On the other hand, many efforts were made by previous researchers to simplify the thermal model of power electronics using equivalent thermal resistances and capacitances circuit [17]–[19]. Although the simplified equivalent thermal circuit is precise, a large amount of analysis and measurement are needed. It is not suited for complex system needs a quick estimate.

To overcome the above limitations, this paper proposes a multi-physics simulation-based virtual prototyping method to design a low-voltage high-current pulse power supply for EAM application. The proposed modeling and design process is shown in Fig. 1. The main contributions are 1) converter-level static and dynamic electro-thermal modeling to support the model-based design; 2) a simplified thermal modeling method to decouple the static thermal modeling and dynamic thermal modeling which significantly reduces the computation time; 3) a selection strategy of power devices for pulse power equipment based on the proposed thermal model. The proposed method is demonstrated by a case study of 10 V/500 A high current pulse power supply. The paper is organized as follows: Section II introduces the case study and key component design based on the electrical performance requirements; Section III discusses the finite element modeling (FEM); Section IV presents the proposed thermal modeling method and the thermal aspect design for the power supply, followed by the conclusions.

II. MAIN CIRCUIT DESIGN

According to the application, the input of EAM pulse power supply is connected to 380 V three-phase power source at

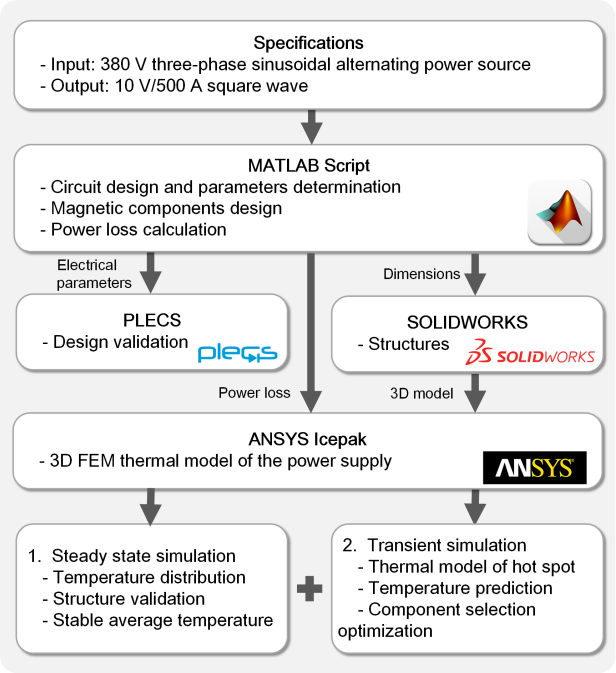

FIGURE 1. Flowchart of the proposed modeling and design process. (The logos of the software are the property of the respective companies).

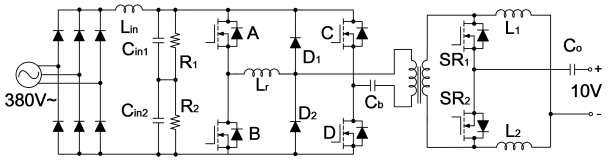

FIGURE 2. Schematic of the main circuit.

TABLE 1. Specifications of the power supply.

Symbol	Description	Value
V_{in}	input voltage	380 V
V_0	maximum output voltage	10 V
I_0	maximum output current	500 A
$\Delta I_{L1}\%$	inductor current ripple	20%
$\Delta V_c\%$	output capacitor voltage ripple	2%

a frequency of 50 Hz, and the output is a continuously adjustable square wave. The load of the power supply in EAM application is usually bone shape metal workpiece. The resistance of the load depends on the size, material, and shape of the workpiece. In this work, a workpiece made of non-crystalline material with a resistance of 0.02 Ω is used. The specifications of the power supply are shown in Table 1.

The schematic diagram of the main circuit is shown in Fig. 2. In the left part, an AC/DC rectifier achieves power factor correction and regulates the bus voltage to a dc value. In the rest of the circuit, the dc-dc stage must step down the voltage and provide a galvanically isolated and tightly regulated dc output. Full-bridge converter is chosen because of the high power (5 kW), and phase-shift control is adopted because of its easy realization of ZVS switching, which can effectively decrease switching loss in a high-frequency device [21]. Clamping diodes D_1 and D_2 are used to suppress voltage spikes in the secondary-side rectifier circuit due to

parasitic oscillations. A current doubler rectifier (CDR) is applied instead of the central tapped rectifier to increase its output current capacity [20]. Synchronous rectification (SR) is used to reduce power loss. L_r is resonant inductor to achieve ZVS. But it is omitted because the leakage inductance of the transformer (about 2 μH) is high enough to meet the energy requirements.

The operation principle and component sizing procedure are based on [21]. The switching frequency of the PSFB is considered as a design variable since it has a significant impact on the efficiency and power density of the converter. In the following study, a switching frequency for every 10 kHz in the range of 10 kHz to 100 kHz is considered. The number of winding turns of the transformer and power losses of every component are calculated under every frequency. A higher frequency would lead to a smaller number of turns, and would subsequently lead to a smaller transformer volume and winding loss. The frequency and number of winding turns are listed in Table 2. However, a higher frequency would also lead to other disadvantages, such as higher power loss of the primary MOSFETs and smaller skin depth in the winding. According to Table 2, 50 kHz is selected for the main circuit. The ultimate parameters of the selected main components are listed in Table 3.

TABLE 2. Frequency and winding turns.

Frequency (kHz)	Primary winding turns	Secondary winding turns
10	100	5
20	60	3
30	40	2
40	40	2
50	20	1
60	20	1
70	20	1
80	20	1
90	20	1
100	20	1

The design of magnetic components is vital since their power losses and dimensions are necessary for the converter-level thermal modeling. For the transformer, Litz wire is used in the primary winding to avoid extra copper loss caused by skin effect. The wire size and strand are calculated based on the American wire gauge (AWG) [22]. Copper foil is adopted in the secondary winding to reduce copper loss under high current. The current density in copper foil is limited to 6 A/mm^2. An empirical coefficient of window utilization factor $K_u = 0.3$ to ensure the selected core able to meet the winding requirements. The inductors are designed according to the procedure in [23].

Based on the voltage and current stresses, specific devices are selected for the circuit. Two MOSFETs are connected in parallel in the synchronous rectifier to share the current. The power losses of the power devices are calculated with the rms current and the electrical parameters from datasheet. The input three-phase diode-bridge rectifier, the primary-side MOSFETs, and the secondary-side MOSFETs have been placed on three separate heat sinks, respectively. As for magnetic components, the power losses consist of core loss and copper loss. The core loss is estimated by empirical equation provided by manufacturers [24], [25],

$$P_{core.XFMR} = 3.5 \cdot f^{1.4} \cdot {B_{\max}}^{2.5} \cdot (0.88 - 0.013 \cdot T + 0.000142 \cdot T^2) \cdot Vol \quad (1)$$

$$P_{core.L} = 6.5 \cdot f^{1.51} \cdot {B_{\max}}^{1.74} \cdot m \quad (2)$$

Vol is the volume of the core, T is the temperature and m is the mass of the core. The copper loss is calculated using an estimated winding length, wire resistance, and an AC resistance coefficient. More accurate cooling performance is obtained in FEM simulation. The part number of the selected devices and corresponding power losses are listed in Table 4. The efficiency of the main circuit is 95.6%.

Fig. 3 shows the simulation results of the output voltage of the power supply. The start-up process and the steady-state output voltage ripple are shown in the two enlarged figures, respectively. It shows that the start-up time is less than 0.2 ms, and the voltage ripple is about 0.1 V (1%).

TABLE 3. Parameters of the main circuit.

Symbol	Description	Value
Preceding Stage		
$I_{in.rms}$	input rms current of rectifier bridge	8.43 A
C_{in1}, C_{in2}	input capacitor	1199 μF
R_1, R_2	smoothing reactor	27 kΩ
L_{in}	input filter inductor	1.65 mH
$B_{max.Lin}$	maximum magnetic flux density	1.5 T
N_{Lin}	turns of inductor winding (single turn wire)	68
S_{Lin}	wire size (AWG)	8
Transformer		
B_{max}	maximum magnetic flux density	0.2717 T
N_p	turns of primary winding (litz wire)	20
S_p	strand size (AWG) of primary winding	$\geq$23
$I_{pri.rms}$	rms current of primary winding	12.5 A
N_s	turns of secondary winding (copper foil)	1
$I_{sec.rms}$	rms current of secondary winding	220.8 A
L_k	leakage inductance	2 μH
Phase Shift Full Bridge (PSFB)		
ph_{eff}	effective phase shift	0.3899
$IS.rms$	rms current of primary-side MOSFET	8.84 A
C_b	DC isolating capacitor	1.9 μF
Synchronous Rectifier (SR))		
$I_{S.rms}$	rms current of SR MOSFET	333.5 A
C_{out}	output capacitor	1100 μF
Output Filter Inductor		
$B_{max.L1}$	maximum magnetic flux density	0.8 T
L_1, L_2	filter inductor	2.44 μH
$I_{L.rms}$	rms current of filter inductor	250 A
ΔI_L	filter inductor current ripple	50 A
N_{L1}	turns of inductor winding (copper foil)	4

III. FEM THERMAL SIMULATION

A FEM thermal model is built up in Icepak computational fluid dynamics (CFD) software. The 3-D model of the whole system is drawn in Solidworks, as shown in Fig. 4. Most of the components are screw mounted and should be

TABLE 4. Power losses of the main components.

Component	Power loss	Description
Three phase rectifier bridge	19.8 W	Vishay VS26MT80
Heat sink 1	-	Wakefield 547-95AB
Input filter inductor core	0.4 W	HITACHI AMCC0025
Input filter inductor winding	4.9 W	Single turn wire
Input filter capacitor (×4)	0.72 W	Nichicon LNU2G272MSEG
Primary-side MOSFET (×4)	6.5 W	CREE C3M0030090K
Heat sink 2 (×2)	-	OHMITE C247-050
Transformer core	15.7 W	Magnetics 0F47228EC
Transformer primary winding	3 W	Litz wire
Transformer secondary winding	7.2 W	Copper foil
SR MOSFET (×4)	24.3 W	IXYS IXTN660N04T4
Heat sink 3	-	Wakefield 511-3M
Filter inductor core (×2)	14.8 W	HITACHI AMCC06R3
Filter inductor winding (×2)	7.2 W	Copper foil
Output capacitor	0.14 W	Nichicon LNT1H153MSE

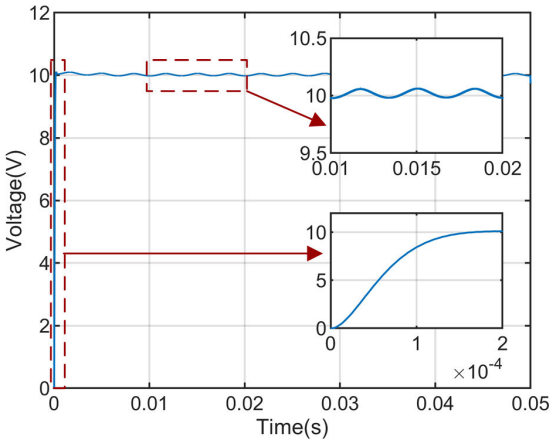

FIGURE 3. Output voltage of circuit simulation result.

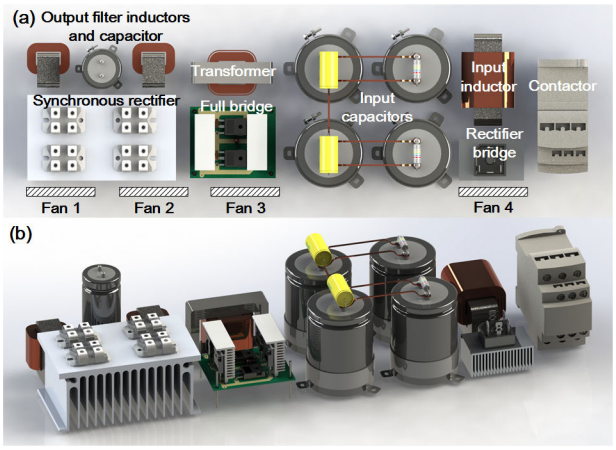

FIGURE 4. The 3-D model of the designed power supply: (a) top view; (b) overall view.

connected with copper bars, which are not included in the model. The 3-D model is then imported into Icepak CFD for the thermal simulation. Some simplification of the structure of the components is done to reduce the complexity of meshing. A schematic diagram of two simplified structures of MOSFET is shown in Fig. 5. The rectifier bridge is simplified

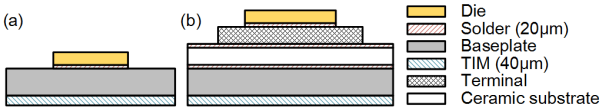

FIGURE 5. Schematic diagram of simplified structures of (a) primary-side MOSFET (b) SR MOSFET.

into the same structure with Fig. 5(a), but with six chips on it according to its real structure. The size of the simplified structures is according to their datasheets. The capacitors are simplified into a metal case and a cylinder core with power loss. The components are restricted in a cuboid cabinet measuring 425 mm×120 mm×140 mm. Four rounded fans with a diameter of 90 mm and flow speed of 19.4 cubic feet per minute (CFM) are adopted on one side of the model, and six 405 mm×5 mm rectangular opening is arranged on the other side for air convection. The position of the fans is marked in Fig. 4.

The power loss data in Table 4 are adopted as Joule heating power in the thermal simulation, and the components are assumed as the heat source in the FEM model. The Joule heating power of the power devices is assumed on the chip. The initial temperature of all the components and ambient air is 60 °C. A steady-state simulation is performed to obtain the stable temperature distribution of all the components in the system in long-term working condition. As the power supply is working in a square wave mode, the Joule heating power defined for each device is an average power loss. The average power loss $\overline{P}_{loss}$ of each component is defined as,

$$\overline{P}_{loss} = P_{loss} \times DUC \tag{3}$$

$$DUC = t_{on}/T_{period} = t_{on}/(t_{on} + t_{off}) \tag{4}$$

For each component, P_{loss} is the calculated power loss. DUC is the on-time ratio (duty cycle) of the square wave output current in one period. t_{on}, t_{off} and T_{period} are the turn-on time, turn-off time and period time of the square wave output current, respectively. The relationship of output current, power loss, average power loss, and the duty cycle is shown in Fig. 6. The maximum output duty cycle of this application is 0.8, which is used in the simulation.

Steady-state simulation in Icepak predicts the airflow velocity and temperature distribution in long-term working condition. The steady-state simulation costs 100 iterations.

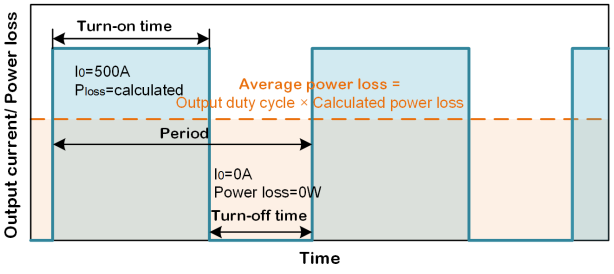

FIGURE 6. The relationship of output current, power loss, average power loss and duty cycle.

TABLE 5. Thermal stress of key components.

Component	Maximum temperature (°C)	Average temperature (°C)
Rectifier bridge die (×6)	75	74
Heat sink 1	71	66
Input filter inductor core	67	67
Input filter inductor winding	72	72
Input filter capacitor (×4)	63	62
Primary-side MOSFET (×4)	91	89
Heat sink 2 (×2)	87	82
Transformer core	95	94
Transformer primary winding	93	90
Transformer secondary winding	97	89
SR MOSFET (×4)	87	85
Heat sink 3	81	75
Filter inductor core 1	119	118
Filter inductor core 2	115	114
Filter inductor Winding 1	118	116
Filter inductor Winding 2	113	112
Output capacitor	65	65

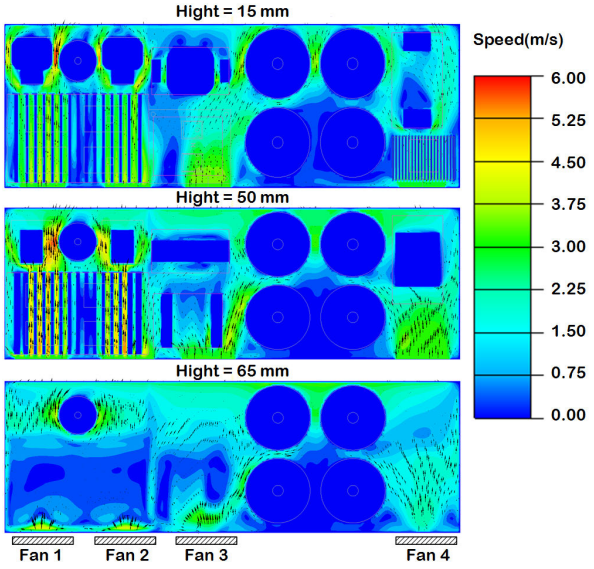

FIGURE 7. Air flow velocity diagram on horizontal intersecting surfaces.

The airflow velocity distribution on several horizontal intersecting surfaces is presented in Fig. 7. It is in the same viewing direction with Fig. 4(a). The maximum temperature and average temperature of the components are listed in Table 5. The temperature of the power switches is represented by the die temperature in the table. All the components work within the operating temperature ranges. The maximum temperature of the primary-side MOSFETs and the SR MOSFETs are 91 °C and 87 °C, which is reasonably below the limits of 150 °C and 175 °C, respectively. Moreover, the capacitors, which are thermal critical, are with a maximum temperature rise of 5 degrees. The temperature distribution of SR MOSFETs and the heat sink attached to them are shown in four intersection surfaces in Fig. 8. These results indicate proper convection (fans and heat sinks) of this system. It implies that the designed power supply can work properly with a maximum duty cycle of 0.8 at an ambient temperature of 60 °C.

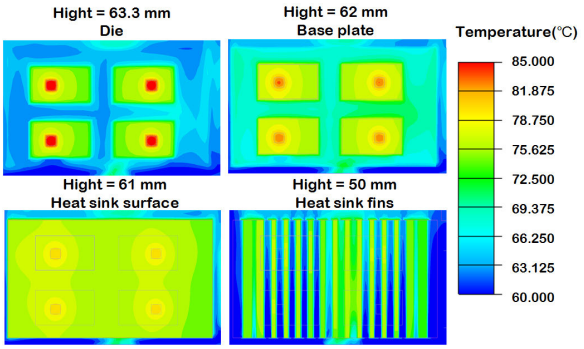

FIGURE 8. Temperature distribution in different intersection surfaces of the SR MOSFETs and the corresponding heat sink.

IV. THERMAL MODEL AND ANALYSIS

The results of circuit simulation and steady-state thermal simulation in Section III have already made a basic design verification. Due to the pulse current operation of the power supply, the temperature fluctuation of the devices should also be considered. The transient temperature variation process can be obtained by defining the loading regulation of power loss in a transient simulation. The thermal characteristic of a system is mainly determined by the structure, material, and convection. The temperature has a certain influence on thermal characteristics, but within the operating temperature range of general equipment, this influence is minimal and can be neglected. That is, a general model can be built for a device in different power loss and environment temperature distribution. Then, the temperature of the device can be predicted without heavy computation burden. According to the power loss in Table 3 and the thermal stress in Table 4, primary-side MOSFETs are the most fragile devices with high working thermal load in the system. Thus, the discussion about the thermal model and the relationship between working pattern and temperature fluctuation focuses on the primary-side MOSFET. This thermal analysis method can also be used for other components in the system. The principle of the thermal modeling is introduced in part A. Temperature prediction and a discussion on device selection based on the thermal model for primary-side MOSFET is presented in part B and C, respectively.

A. PRINCIPLE OF THERMAL MODELING

The temperature-rise process during the heating time of a specific component can be represented by,

$$T_{Heat}(t) = P_{loss} \cdot \sum_{i=1}^{n} A_i \cdot \left(1 - e^{-B_i \cdot t}\right) + T_0 \tag{5}$$

in which T_0 is the initial temperature, n is the order of the thermal model, A_i and B_i are coefficients of the thermal model. Similarly, the cooling process of a specific component is,

$$T_{Cool}(t) = \lambda \cdot \sum_{i=1}^{n} C_i \cdot e^{-D_i \cdot t} + T_0 \tag{6}$$

C_i and D_i are coefficients of the model, and λ is the equivalent heat transfer coefficient. The equivalent heat transfer coefficient has a relationship with the temperature distribution of the environment. In the steady-state operation, the temperature decrease during the cooling time must completely offset the heating during one single pulse. Therefore, λ can be calculated and the temperature fluctuation of one pulse in the steady state can be expressed as,

$$\lambda = \frac{P_{loss} \cdot \sum_{i=1}^{n} A_i \cdot \left(1 - e^{-B_i \cdot t_{on}}\right)}{\sum_{i=1}^{n} C_i \cdot \left(1 - e^{-D_i \cdot t_{off}}\right)} \tag{7}$$

$$T(t) = \begin{cases} P_{loss} \cdot \sum_{i=1}^{n} A_i \cdot \left(1 - e^{-B_i \cdot t}\right) \\ \qquad (0 \le t \le t_{on}) \\ \lambda \cdot \sum_{i=1}^{n} C_i \cdot \left[1 - e^{-D_i \cdot (t - t_{on})}\right] + T(t_{on}) \\ \qquad \left(t_{on} < t \le T_{period}\right) \end{cases} \tag{8}$$

λ is a coefficient depending on power loss and turn-on, turn-off time.

The dynamic thermal profile during the initial heating up period (i.e., before the system reach to the steady-state thermal stress) consists of a DC component representing the overall trend of temperature rise, and an AC component representing the fluctuation of repeated pulse. The AC component is a periodic repetition of (8). Before components reach thermal stability, the DC component is a function of time and average power loss $\overline{P}_{loss}$. The DC component can be acquired by a simple transient simulation with a constant power loss. The temperature curve can derived by adding the DC component and AC component together. The DC component is a constant while the system becomes stable. Thus, the temperature fluctuation of a pulse under steady-state operating can be calculated by adding up a DC component to (8) which is,

$$\begin{aligned} T_{DC}(t) &= T_{steady}(t) - T_{mean} \\ &= T_{steady}(t) - \int_0^{T_{period}} T(t) \cdot dt \Big/ T_{period} \end{aligned} \tag{9}$$

$T_{steady}(t)$ and T_{mean} are the temperature obtained based on a constant power loss and the average temperature of one pulse calculated in (8). In stable state, $T_{steady}(t)$ is a constant temperature from the steady-state simulation result.

B. COEFFICIENT FITTING AND TEMPERATURE PREDICTION

Based on the 3-D FEM model discussed in Section III, a transient temperature simulation with 20 seconds turn-on time and 20 seconds turn-off time is done. The SR MOSFETs, having the highest power loss, is selected for illustration purpose here. Other components in the power supply system maintain their working loads in Table 4 for the first 20 seconds and turn off in the next 20 seconds, which means the thermal coupling behavior with other components are represented in the simulation. The time step is 0.05s from 0 to 1 s, because the temperature changes fast at the beginning. The time step is set to 0.5 s in 1-5 s, 1 s in 5-10 s, and 2 s in 10-20 s. For the turn on and turn off time, 78 calculation time points, 1560 iterations, are used in total.

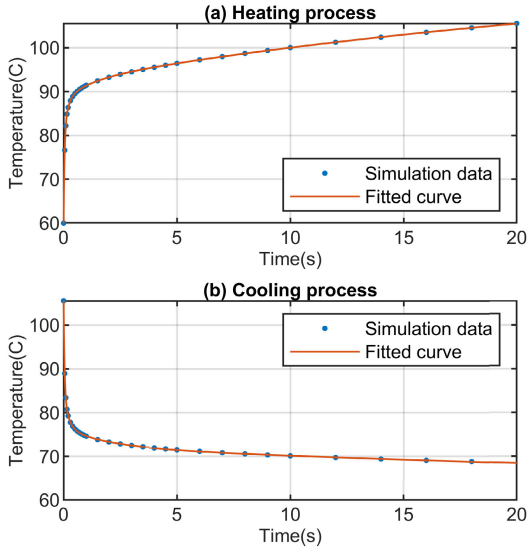

FIGURE 9. Curve fitting of temperature change process of SR MOSFET: (a) heating process (P_{loss} = 64.6 W); (b) cooling process (P_{loss} = 0 W).

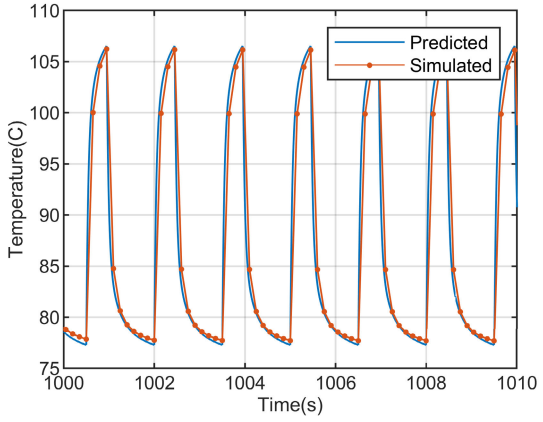

FIGURE 10. Comparison of the model predicted and simulated temperature fluctuation curve of SR MOSFET (P_{loss} = 64.6 W, t_{on} = 0.45 s, t_{off} = 1.05 s).

The temperature variation of the SR MOSFET is extracted from the simulation results. The temperature data can be divided into a heating process (0-20 s) and a cooling process (20-40 s), and are plotted in Fig. 9 with dots. The two curves are fitted with (5) and (6), respectively, with a fourth-order model. The fitting curve is also plotted in Fig. 9, and the comparison shows excellent consistency. The fitted coefficients are listed in Table 6.

By using this thermal model, temperature variation in different situations can be obtained. The results of one square wave loading situation are chosen as an illustration. The model predicted and FEM simulated temperature fluctuation curves (in stable state) are compared in Fig. 10.

TABLE 6. Thermal model coefficient.

Order	A	B	C	D
1	0.4183	0.0333	12.2	0.01836
2	0.06391	0.8003	4.366	0.51
3	0.1342	5.937	8.281	4.829
4	0.3023	25.65	20.68	24.47

The comparison error between these two curves is less than 1°C, which proves the validity of the derived thermal model.

The simulated temperature curve in Fig. 10 is derived from an unsimplified rigorous transient CFD simulation. The time span is 1200 seconds to make sure the system achieve stability. The system needs at least 500 seconds before stability. The time step should be smaller than 1 s to know the details of temperature change. That is, a rigorous simulation costs at least 10000 iterations, which means the simplified thermal model reduced at least 83% computational burden. The rigorous simulation in Fig. 10 costs 160000 iterations, and the simplified thermal model reduced 99% of the computational burden.

C. DISCUSSION ON DEVICE SELECTION

In EAM application, the typical on-time of the periodic pulse current is less than 2 s, and the duty cycle is usually less than 0.5. Due to this feature, the maximum junction temperature of MOSFETs may be lower than that under continuous current operation due to its thermal capacitance. This sub-section discusses the maximum allowable on-time of the pulse current with different choices of MOSFETs.

Several alternative MOSFETs are selected with the SOT-227 package. Their on-state resistance are 1.9 mΩ, 2.3 mΩ and 2.6 mΩ, respectively. Their power losses are calculated as 53.5 W, 64.6 W and 73.0 W compared to 24.3 W of the initial selected MOSFETs. Their maximum duty cycles are 0.36, 0.3, and 0.27, respectively, to maintain a same average power loss in (3). The junction temperature fluctuation in a period is,

$$\Delta T = P_{loss} \cdot \sum_{i=1}^{n} A_i \cdot \left(1 - e^{-B_i \cdot t_{on}}\right) \tag{10}$$

For a given certain maximum junction temperature fluctuation ΔT, the maximum turn-on time can be obtained from 10. If the maximum junction temperature variation is limited to 25 °C, as an example, the temperature variation of one single pulse of these MOSFETs can be obtained using the thermal model. The results are plotted in Fig. 11. The maximum turn-on time are 0.63 s, 0.15 s, 0.10 s, respectively. That is, if the turn-on time is less than 0.63 s and the duty cycle is smaller than 0.36, the SR MOSFET can be replaced by the one with 53.5 W power loss. The feasible range of different MOSFETs is shown in Table 7. Therefore, different devices can be selected for the power supply based on this result and the application requirements.

As a summary, this method can be described as several steps: 1) a steady-state FEM simulation using average power loss for the first step thermal design, to ensure the designed power supply is feasible for a long-term operation; 2) for the component need to discuss, find several alternative options with the same packaging, and calculate their power loss; 3) a transient FEM simulation (20 s heating and 20 s cooling) using one of the selected options, and obtain the parameters for the thermal model; 4) for a required maximum temperature fluctuation, obtained the maximum turn-on time and maximum duty cycle for each alternative option using the thermal model. Then, the most suitable component is found according to the design requirements. The thermal model can be applied to all the components in the designed equipment. The temperature prediction with the proposed thermal model is not as precise as the RC thermal circuit, but is more convenient especially for a preproduction analysis and verification. The device selection strategy is more suitable for power switches with high power loss, and the optional devices should have the same package.

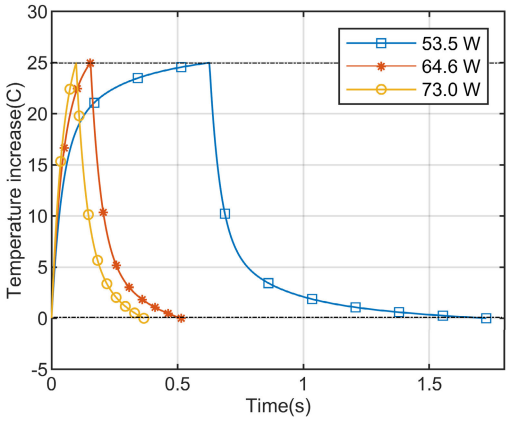

FIGURE 11. Temperature curve of different MOSFETs With the same maximum temperature change (ΔT = 25°C) obtained by proposed model.

TABLE 7. Feasible range of alternative MOSFETs.

Conduction resistance ($R_{ds,on}$)	Power loss (P_{loss})	Maximum duty cycle (DUC)	Maximum turn-on time ($\Delta T = 25°C$)	Maximum turn-on time ($\Delta T = 30°C$)
0.85 mΩ	24.3 W	0.80	No restriction	No restriction
1.9 mΩ	53.5 W	0.36	0.63 s	4.78 s
2.3 mΩ	64.6 W	0.30	0.15 s	0.58 s
2.6 mΩ	73.0 W	0.27	0.10 s	0.22 s

V. CONCLUSION

The electro-thermal modeling and design of key components of a high-current pulse supply have been presented in this paper. Based on the power loss analysis and converter-level thermal simulation, curve-fitted thermal models can be obtained to ensure proper design margins and to optimize the sizing of key components, such as MOSFETs. Moreover, a method to reduce the computation burden of the FEM simulation is presented to obtain the dynamic thermal profile under pulse current operation.

A case study of a 5 kW 500 A pulse supply is demonstrated. The circuit is first designed, and a FEM simulation is built based on the calculated power losses. A simplified thermal model of one representative component is proposed with the transient temperature results from the FEM simulation, to achieve the dynamic temperature prediction.

The difference between the obtained thermal results from the FEM simulations and calculations is less than 1 °C. The simplified model reduces at least 83% of the computational burden. A component selection strategy is presented based on the proposed thermal model. The presented study provides the model-based design and optimization of power supplies for electrically assisted manufacturing (EAM) applications.

REFERENCES

[1] B. J. Ruszkiewicz, T. Grimm, I. Ragai, L. Mears, and J. T. Roth, "A review of electrically-assisted manufacturing with emphasis on modeling and understanding of the electroplastic effect," *J. Manuf. Sci. Eng.*, vol. 139, no. 11, Nov. 2017, Art. no. 110801.
[2] W. A. Salandro, J. J. Jones, C. Bunget, L. Mears, and J. T. Roth, "Introduction to electrically assisted forming" in *Electrically Assisted Forming*. New York, NY, USA: Springer, 2014, pp. 23–36.
[3] H. D. Nguyen-Tran, H. S. Oh, S. T. Hong, H. N. Han, J. Cao, S. H. Ahn, and D. M. Chun, "A review of electrically-assisted manufacturing," *Int. J. Precis. Eng. Manuf.-Green Technol.*, vol. 2, no. 4, pp. 365–376, Oct. 2015.
[4] O. A. Troitskii, "Effect of the electron state of a metal on its mechanical properties and the phenomenon of electroplasticity," *Strength Mater.*, vol. 9, no. 1, pp. 35–45, Jan. 1977.
[5] X. Li, S. Wang, S. Zhao, W. Ding, J. Chen, and G. Wu, "Effect of pulse current on the tensile deformation of SUS304 stainless steel," *J. Mater. Eng. Perform.*, vol. 24, no. 12, pp. 5065–5070, Dec. 2015.
[6] J.-H. Roh, J.-J. Seo, S.-T. Hong, M.-J. Kim, H. N. Han, and J. T. Roth, "The mechanical behavior of 5052-H32 aluminum alloys under a pulsed electric current," *Int. J. Plasticity*, vol. 58, no. 5, pp. 84–99, Jul. 2014.
[7] S. Samuha, E. Kahana, O. Sadot, and R. Z. Shneck, "Improved formability of Mg-AZ80 alloy under a high strain rate in expanding-ring experiments," *Materials*, vol. 11, no. 2, p. 329, Feb. 2018.
[8] V. V. Stolyarov, "Electroplastic effect in nanocrystalline and amorphous alloys," *Mater. Sci. Technol.*, vol. 31, no. 13, pp. 1536–1540, 2015.
[9] H.-W. Li, S.-L. Yan, M. Zhan, and X. Zhang, "Eddy current induced dynamic deformation behaviors of aluminum alloy during EMF: Modeling and quantitative characterization," *J. Mater. Process. Technol.*, vol. 263, pp. 423–439, Jan. 2019.
[10] S. Yang, A. Bryant, P. Mawby, D. Xiang, L. Ran, and P. Tavner, "An industry-based survey of reliability in power electronic converters," *IEEE Trans. Ind. Appl.*, vol. 47, no. 3, pp. 1441–1451, May/Jun. 2011.
[11] H. Wang and F. Blaabjerg, "Reliability of capacitors for DC-link applications in power electronic converters—An overview," *IEEE Trans. Ind. Appl.*, vol. 50, no. 5, pp. 3569–3578, Sep./Oct. 2014.
[12] R. W. Johnson, C. Wang, Y. Liu, and J. D. Scofield, "Power device packaging technologies for extreme environments," *IEEE Trans. Electron. Packag. Manuf.*, vol. 30, no. 3, pp. 182–193, Jul. 2007.
[13] X. Han, L. Huang, J. Shi, B. Ni, X. Duan, and Q. Chen, "Development of mechanical measurement system applied for electroplastic effect research," in *Proc. I2MTC*, Montevideo, Uruguay, May 2014, pp. 945–948.
[14] K. Deng and M. He, "Study on thermal design of high-power power supply with synchronous rectifiers," *AIP Conf. Proc.*, vol. 1864, no. 1, 2017, Art. no. 020211.
[15] G. Breglio, A. Irace, L. Maresca, and M. Riccio, "Electro-thermal simulations of power semiconductor devices during high stress events," in *Proc. ESARS-ITEC*, Nottingham, U.K., Nov. 2018, pp. 1–4.
[16] R. J. P. Lima, L. Luppi, P. A. C. Rocha, M. E. V. da Silva, C. M. T. Cruz, and S. P. Mendonça, "Experimental measurements and computational simulation (computational fluid dynamics) applied for thermal analysis of an uninterruptible power supply," *Comput. Therm. Sci., Int. J.*, vol. 11, no. 4, pp. 353–366, 2019.
[17] A. S. Bahman, K. Ma, and F. Blaabjerg, "A lumped thermal model including thermal coupling and thermal boundary conditions for high-power IGBT modules," *IEEE Trans. Power Electron.*, vol. 33, no. 3, pp. 2518–2530, Mar. 2018.
[18] K. Ma, N. He, M. Liserre, and F. Blaabjerg, "Frequency-domain thermal modeling and characterization of power semiconductor devices," *IEEE Trans. Power Electron.*, vol. 31, no. 10, pp. 7183–7193, Oct. 2016.
[19] P. Chatzipanagiotou and V. Chatziathanasiou, "Dynamic thermal analysis of a power line by simplified RC model networks: Theoretical and experimental analysis," *Int. J. Electr. Power Energy Syst.*, vol. 106, pp. 288–293, Mar. 2019.
[20] P. Alou, J. A. Oliver, O. Garcia, R. Prieto, and J. A. Cobos, "Comparison of current doubler rectifier and center tapped rectifier for low voltage applications," in *Proc. Annu. IEEE Appl. Power Electron. Conf. Expo. (APEC)*, Dallas, TX, USA, Mar. 2006, pp. 744–750.
[21] S. A. Rahman, "Design of phase shifted full-bridge converter with current doubler rectifier," in *Proc. Infineon Technol.*, 2013, pp. 1–9.
[22] C. R. Sullivan, "Optimal choice for number of strands in a litz-wire transformer winding," in *Proc. Annu. IEEE Power Electron. Spec. Conf. (PESC97)*, Saint Louis, MO, USA, Jun. 1997, pp. 28–35, doi: 10.1109/PESC.1997.616632.
[23] R. W. Erickson and D. Maksimović, "Inductor design," in *Fundamentals Power Electronics*. New York, NY, USA: Springer, 2007, pp. 539–564.
[24] *Magnetics Ferrite Core Loss Calculator*. Accesse: Jun. 2013. [Online]. Available: https://www.mag-inc.com/Design/Design-Guides/Ferrite-Core-Loss-Calculator
[25] Hitachi Metals. *Powerlite Inductor Cores*. Accessed: Apr. 2011. [Online]. Available: https://www.hitachimetals.com/materials-products/amorphous-nanocrystalline/powerlite-c-cores/documents/POWERLITE_C_opt.pdf

JIAWEI WU was born in Wuhan, China in 1993. She received the B.S. degree in electrical and electronics engineering from the Huazhong University of Science and Technology, Wuhan, China, in 2015, where she is currently pursuing the Ph.D. degree with the Wuhan National High Magnetic Field Center.

She was a visiting Ph.D. student at Aalborg University, Denmark, from September 2018 to August 2019. Her principal research interests include electromagnetic forming, multiphysics simulation, electromagnetic analysis, and power electronics.

XIAOTAO HAN received the B.S. and Ph.D. degrees in electrical and electronics engineering from the Huazhong University of Science and Technology, Wuhan, China, in 1996 and 2004, respectively.

From July 2005 to October 2011, he was with the College of Electrical and Electronic Engineering, Huazhong University of Science and Technology, where he is currently a Professor. Since November 2011, he has been with the Wuhan National High Magnetic Field Center. His principal research interests include electromagnetic measurements, signal processing, and application technology of the high magnetic field.

HUAI WANG (M'12–SM'17) received the B.E. degree in electrical engineering from the Huazhong University of Science and Technology, Wuhan, China, in 2007, and the Ph.D. degree in power electronics from the City University of Hong Kong, Hong Kong, in 2012.

He was with the ABB Corporate Research Center, Switzerland, in 2009. He was a Visiting Scientist with the Massachusetts Institute of Technology (MIT), USA, from September to November 2013, and ETH Zurich, Switzerland, from August to September 2014. He is currently a Professor with the Center of Reliable Power Electronics (CORPE), Department of Energy Technology, Aalborg University, Denmark. His research interests include the fundamental challenges in modeling and validation of power electronic component failure mechanisms, and application issues in system-level predictability, condition monitoring, circuit architecture, and robustness design.

Dr. Wang was a recipient of the Richard M. Bass Outstanding Young Power Electronics Engineer Award from the IEEE Power Electronics Society, in 2016, and the Green Talents Award from the German Federal Ministry of Education and Research, in 2014. He is currently the Chair of the IEEE PELS/IAS/IES Chapter in Denmark. He serves as an Associate Editor of *IET Electronics Letters*, the IEEE JOURNAL OF EMERGING AND SELECTED TOPICS IN POWER ELECTRONICS, and the IEEE TRANSACTIONS ON POWER ELECTRONICS.